

Individual Tree Species Classification From Airborne Multisensor Imagery Using Robust PCA

Juheon Lee, Xiaohao Cai, Jan Lellmann, Michele Dalponte, Yadvinder Malhi, Nathalie Butt, Mike Morecroft, Carola-Bibiane Schönlieb, and David A. Coomes

Abstract—Remote sensing of individual tree species has many applications in resource management, biodiversity assessment, and conservation. Airborne remote sensing using light detection and ranging (LiDAR) and hyperspectral sensors has been used extensively to extract biophysical traits of vegetation and to detect species. However, its application for individual tree mapping remains limited due to the technical challenges of precise coalignment of images acquired from different sensors and accurately delineating individual tree crowns (ITCs). In this study, we developed a generic workflow to map tree species at ITC level from hyperspectral imagery and LiDAR data using a combination of well established and recently developed techniques. The workflow uses a nonparametric image registration approach to coaligned images, a multiclass normalized graph cut method for ITC delineation, robust principal component analysis for feature extraction, and support vector machine for species classification. This workflow allows us to automatically map tree species at both pixel- and ITC-level. Experimental tests of the technique were conducted using ground data collected from a fully mapped temperate woodland in the UK.

Manuscript received October 10, 2015; revised January 11, 2016, March 19, 2016, and April 25, 2016; accepted April 29, 2016. Date of publication June 25, 2016; date of current version July 05, 2016. This work was supported by a Grant from DEFRA/BBSRC to study the spread of ash dieback in British woodlands, and a Grant from the Isaac Newton Trust. (*Corresponding author:* Juheon Lee).

J. Lee is with the Forest Ecology and Conservation Group, Department of Plant Sciences, University of Cambridge, Cambridge CB2 3EA, U.K., and also with the Image Analysis Group, Department of Applied Mathematics and Theoretical Physics, University of Cambridge, Cambridge CB3 0WA, U.K. (e-mail: jl626@cam.ac.uk).

X. Cai is with the Forest Ecology and Conservation Group, Department of Plant Sciences, University of Cambridge, Cambridge CB2 3EA, U.K., and with the Image Analysis Group, Department of Applied Mathematics and Theoretical Physics, University of Cambridge, Cambridge CB3 0WA, U.K., and also with the Mullard Space Science Laboratory, University College London, Surrey RH5 6NT, U.K. (e-mail: xc274@cam.ac.uk).

J. Lellmann and C.-B. Schönlieb are with the Image Analysis Group, Department of Applied Mathematics and Theoretical Physics, University of Cambridge, Cambridge CB3 0WA, U.K. (e-mail: jl707@cam.ac.uk; cbs31@cam.ac.uk).

M. Dalponte is with the Forest Ecology and Conservation Group, Department of Plant Sciences, University of Cambridge, Cambridge CB2 3EA, U.K., and also with the Department of Sustainable Agro-Ecosystems and Bioresources, Research and Innovation Centre, Fondazione E. Mach, San Michele all'Adige 38010, Italy (e-mail: michele.dalponte@fmach.it).

Y. Malhi is with the Environmental Change Institute, School of Geography and the Environment, University of Oxford, Oxford OX1 3QY, U.K. (e-mail: yadvinder.malhi@ouce.ox.ac.uk).

N. Butt is with the Environmental Change Institute, School of Geography and the Environment, University of Oxford, Oxford OX1 3QY U.K., and also with the Centre for Biodiversity and Conservation Science, The University of Queensland, St Lucia, Qld 4072, Australia (e-mail: n.but@uq.edu.au).

M. Morecroft is with the Natural England, Cromwell House, Winchester SO23 7BT, U.K. (e-mail: Mike.Morecroft@naturalengland.org.uk).

D. A. Coomes is with the Forest Ecology and Conservation Group, Department of Plant Sciences, University of Cambridge, Cambridge CB2 3EA, U.K. (e-mail: dac18@cam.ac.uk).

Color versions of one or more of the figures in this paper are available online at <http://ieeexplore.ieee.org>.

Digital Object Identifier 10.1109/JSTARS.2016.2569408

The overall accuracy of pixel-level classification was 91%, while that of ITC-level classification was 61%. The test results demonstrate the effectiveness of the approach, and in particular the use of robust principal component analysis to prune the hyperspectral dataset and reveal subtle difference among species.

Index Terms—Hyperspectral imaging, image registration, image segmentation, light detection and ranging (LiDAR), principal component analysis (PCA), species classification, support vector machine (SVM), Wytham Woods.

I. INTRODUCTION

HAVING maps of individual tree locations is fundamental to understanding forest responses to global change, providing a basis for monitoring species distribution patterns, responses to stress, disease, and exotic-species spread and deforestation [1]. Mapping species using conventional surveying methods requires a large amount of time and effort. Therefore, few tree maps extend beyond 50-ha. The examples are larger scale maps that have been generated by sampling in small plots distributed over wider regions and interpolating them [2]. The development of sophisticated remote sensing technologies is making it increasingly feasible to monitor single trees in forests alternatively using satellites or aircraft. Satellite-based multispectral sensors, such as WorldView-2, provide high-resolution imagery covering visible and near infrared channels. These sensors are increasingly used for mapping species, but their effectiveness in species discrimination varies from study to study due to limited spectral resolution [3]–[6]. Airborne hyperspectral sensors, on the other hand, can measure spectral properties of a target in narrow bands ranging from visible to short-wave infrared (SWIR) wavelengths of the electromagnetic spectrum (400–2500 nm). Studies carried out with handheld hyperspectrometers show that species are often distinguishable from their leaf reflectance spectra, even in diverse tropical forests [7], [8]. For example, about half of 188 species sampled from a humid tropical forest in Hawaii could be distinguished from their spectra, with differential reflectance in the SWIR as well as the visible and new infrared (NIR) being important [8], [9]. Such results prognosticate the usability of remote sensing with similar sensors for identification of individual trees [10]–[13].

Airborne hyperspectral imaging provides spectral properties of the vegetation canopies, which can be used to identify tree species. Scaling-up species classification from leaf level to canopy level remains challenging as reflectance signals of mixed vegetation canopy are influenced by leaf density, leaf angle distribution, crown shape, and shading [12]. Nevertheless, recent studies have successfully used hyperspectral imaging to map species in tropical forests [9], [14],

[15], savanna woodlands [16], [17], Mediterranean woodlands [18], [19], temperate deciduous forests [20]–[22], and boreal forests [23], [24]. Clark *et al.* [14] pioneered the use of hyperspectral data to identify canopy species in tropical rain forest, detecting seven tree species with 92% accuracy. Cho *et al.* [25] detected ten tree species with 57% accuracy in the lowveld woodlands of South Africa. Dalponte *et al.* [18] classified 23 species from two Mediterranean woodlands, and achieved 88% and 96% accuracy for those regions. Therefore, rapid advances are being made in this context.

The accuracy of pixel-level species maps can be improved by combining features from light detection and ranging (LiDAR) and hyperspectral imagery in classification algorithms. LiDAR produces three-dimensional (3-D) point clouds indicating tree positions, from which canopy height and various other metrics can be extracted for each pixel. Features comprised of this structural information complement the optical data provided by hyperspectral sensors, particularly as LiDAR data are not influenced by illumination artifacts such as shading of shorter trees by their taller neighbors [26]. High species classification accuracy (89%) in an Italian temperate floodplain forest was achieved by fusing LiDAR and hyperspectral imagery before classification [26]. Jones *et al.* [27] showed that LiDAR and hyperspectral fusion can improve species classification in a mixed broadleaf-conifer forest. The work of Dalponte *et al.* [28] also showed that improvement was observed when LiDAR and hyperspectral imagery were used together in alpine forests containing a mixture of beech and conifers. However, the importance of LiDAR-derived features on classification success varies greatly among species [27]–[29].

The approaches described above illustrate the advances made in pixel-based classification, but less progress has been made in mapping individual tree crowns (ITCs) using multisensor techniques. The LiDAR 3-D point cloud provides excellent data for ITC delineation [26]–[30], while canopy spectral information can be obtained from the corresponding pixels of hyperspectral imagery within each of the identified crowns, so in principle this combination of information is powerful [25], [31]–[35]. Mapping species at a single tree scale has been demonstrated in urban environments, where trees are sparsely distributed [32]–[34], [36]. For example, Alonzo *et al.* [34] mapped 30 urban tree species at ITC level using full spectral bands of hyperspectral imagery and seven tree structural parameters derived from LiDAR. However, for more complex environments, we know of only four studies that have investigated ITC-level species classification using a multisensor approach: Colgan *et al.* delineated ITCs from LiDAR and classified species from hyperspectral imagery in a savanna woodland, then combined these results [25]. Dinuls *et al.* [37] extracted tree tops from LiDAR, then classified five species from corresponding pixels taken from multispectral imagery. Heinzel and Koch showed that under-segmentation of ITCs using LiDAR-based delineation could be rectified by using species classification information alongside LiDAR [31]. Dalponte *et al.* improved species classification by only selecting pixels inside of ITCs in the training step of the classification [35]. Matsuki *et al.* [22] showed that LiDAR-

derived ITC features and shade correction of hyperspectral imagery could improve the accuracy of species classification. So this sort of analysis is still in its infancy.

This paper develops a generic workflow for tree species classification at ITC level from LiDAR and hyperspectral sensors. We deal with several technical challenges:

- 1) Multisensor imaging requires images recorded by various sensors need to be coaligned. This is complicated by the fact that different sensor characteristics result in scale, rotation, or translation mismatches between images, making correction a prerequisite. Our workflow includes an image registration step using the NGF-Curv method [38] to coalign hyperspectral imagery and LiDAR.
- 2) Locating ITCs in the 3-D LiDAR point cloud or optical imagery requires an accurate tree delineation algorithm, but most established approaches are inaccurate in broadleaf forests [30], [39]. Our workflow includes a normalized graph cut scheme to delineate ITCs using LiDAR 3-D point cloud information alongside optical imagery [40]. The effectiveness of our workflow will be demonstrated in a broadleaf forest.
- 3) When selecting features for the classification, it is recognized that the dimensionality of hyperspectral data must be reduced to improve computationally efficiency. Moreover hyperspectral imagery may have a significant noise component, which make this selection challenging. We use robust principal component analysis (rPCA) to prune the data, strip away some of the noise and select the most important features for the classification only [41].
- 4) Finally, the tree species classification at both pixel level and ITC level is implemented using a support vector machine (SVM) [42].

The main contribution of this paper is the development of a systematic workflow to map tree species at both pixel level and ITC level from multisensor imagery utilizing a combination of new and established approaches, which provide a powerful new approach for tree mapping. We test the efficiency of this approach by working with airborne imagery collected over a 18-ha mapped stand of temperate woodland in the UK. Historically managed temperate forests are recognized as being particularly difficult for ITC delineation because they have relatively even upper canopies comprised of intercalated crowns. To the best of our knowledge, only four studies have explored ITC-level species classification in a temperate forest [4], [22], [31], [37].

The paper is organized as follows: in Section II, we introduce the temperate forest datasets tested in this paper. In Section III, we present our workflow for tree species classification at both pixel level and ITC level from LiDAR and hyperspectral sensors. The results and discussion are shown in Section IV. Conclusion and outlook are given in Section VI.

II. DATA DESCRIPTION

A. Study Site and Field Data

Wytham Woods is a 385-ha deciduous forest, located in Oxfordshire, England ($51^{\circ} 46' N$, $1^{\circ} 20' W$). A 18-ha forest plot was established in this wood in 2008 using standardized

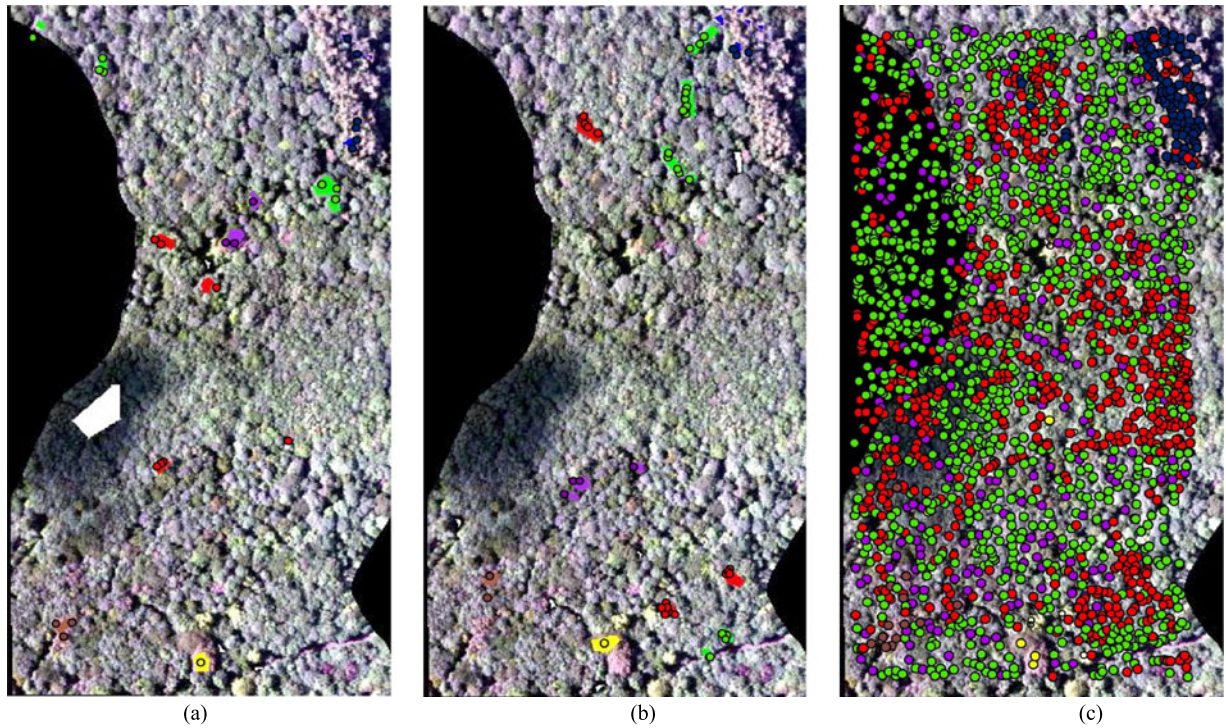


Fig. 1. Training and testing samples for species classification in Wytham Woods. The colored points in panel (a), (b), and (c) are ground truth overlaid over a false color representation of the hyperspectral imagery. The colored polygons in (a) and (b) represent training and testing samples of each species overlaid over a false color representation of the hyperspectral imagery. Colors indicate different species, i.e., blue = *Larix decidua*, green = *Acer pseudoplatanus*, red = *Fraxinus excelsior*, yellow = *Fagus sylvatica*, purple = *Quercus robur*, brown = *Betula* spp., and white = shaded pixels.

TABLE I
NUMBERS OF INDIVIDUAL AND CANOPY TREES OF SIX SPECIES RECORDED IN
WYTHAM PLOT

Species	Common name	No. of individual trees	No. of canopy trees
<i>Fraxinus excelsior</i>	European ash	5346	1249
<i>Acer pseudoplatanus</i>	Sycamore	7716	778
<i>Larix decidua</i>	European larch	99	98
<i>Quercus robur</i>	English oak	381	201
<i>Fagus sylvatica</i>	European beech	195	4
<i>Betula</i> spp.	Birch	85	16

methods used in an international network of Smithsonian Institution Global Earth Observatories (SIGEO) [43]. Each hectare was delimited into 25 subplots of 20 m × 20 m. Every tree larger than 5-cm diameter at chest height (DBH) was tagged, its DBH measured, its species identified and its location mapped. There were 23 species of tree and shrub within the plot. In total, 20 308 stems and 16 313 individual trees were recorded (some trees had multiple stems). These plots were recensused in 2009 and 2012, and the latest dataset was used in this study.

As subcanopy species and shrubs are hard to detect by remote sensing, this study focuses on mapping the six most dominant canopy tree species listed in Table I. Fig. 1 shows the linkage between field data, and training and testing samples taken from the airborne survey. Tree height information is an important indicator for ITC-level species mapping. However, it was only measured on 389 individuals of these dominant canopy tree species. Species-specific functions were fitted to the height–diameters

relationships ($H = a \ln DBH + b$, where a and b are coefficients estimated by linear regression) and these functions were used to estimate tree height information from DBH. We arbitrarily labeled trees >18-m height as “canopy trees” (see Table I) and used these to assess the accuracy of species detection.

B. Airborne Survey

Airborne surveying was conducted in the Wytham Woods natural reserve on June 24, 2014 by the Airborne Research and Survey Facility of the UK Natural Environment Research Council (NERC-ARSF). The airplane flew at a nominal height above ground of approximate 800 m and was equipped with LiDAR and hyperspectral imagers. LiDAR and hyperspectral imagery were preprocessed by NERC-ARSF Data Analysis Node.

Hyperspectral imagery was obtained by the AISA Fenix sensor, which is a pushbroom imaging array sensor with 384 cross-track pixels and provides 361 spectral bands from visible to SWIR (0.4–2.5 μm) region. The field of view of the AISA Fenix sensor is 31.94°. In this study, a single flight line of hyperspectral imagery was used, so illumination and sensor geometry were similar for all pixels. Atmospheric correction was not applied to the hyperspectral imagery. Although adjacency effects can influence the classification accuracy and atmospheric correction can reduce this problem, a number of studies have reported that applying an atmospheric correction has little effect on species classification [26], [35], [44], [45]. A bidirectional distribution function correction was not applied since a single flight line was used. If the hyperspectral imagery had been obtained from

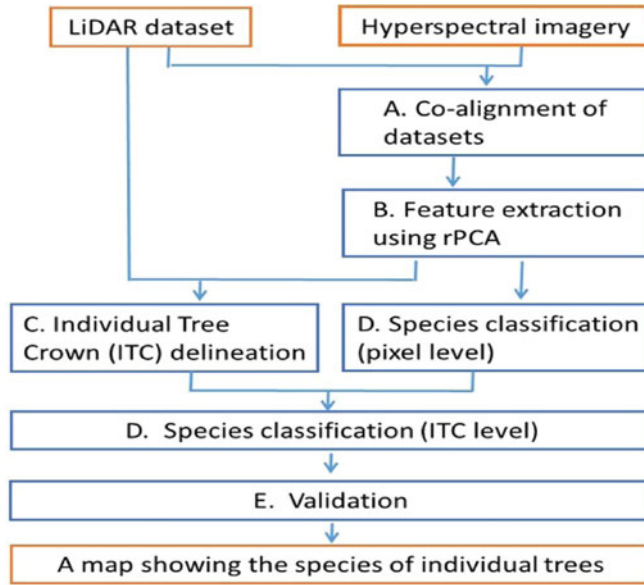


Fig. 2. Workflow used to detect ITC and identify their species by fusing LiDAR and hyperspectral imagery.

several flight lines, radiometric normalisation would have been needed in our workflow (see Fig. 2). The hyperspectral imagery was orthorectified and georeferenced in Ordinary Survey Great Britain (OSGB) projection, with spatial resolution of 1.2 m. The airborne LiDAR data were acquired by the Leica ALS-50 II sensor. A scan angle of 12° was used. The LiDAR data were originally captured in full waveform, however, they were converted to discrete LiDAR point cloud during the preprocessing step, within which the LiDAR point cloud was georeferenced in OSGB projection. The final point density was approximately 6 points/m². The equipment on board the NERC aircraft is regularly calibrated to ensure that LiDAR data are accurately georeferenced and the hyperspectral imagery is radiometrically calibrated before delivery.

III. METHOD

In this section, we present our processing workflow for pixel-level and ITC-level tree species classification from LiDAR and hyperspectral imagery, see Fig. 2. The coalignment step uses the NGF-Curv image registration method [38], the feature extraction from hyperspectral imagery is carried out with the rPCA method [41], the ITC delineation step uses a LiDAR point cloud-based clustering method that is informed by hyperspectral information called MC–RC [40], and, finally, the tree species classification at pixel level and ITC level is conducted with a SVM classifier [42] with the majority voting rule over each delineated crown area. The workflow in Fig. 2 is very general, and the methods are described in greater detail below.

A. Coalignment of LiDAR and Hyperspectral Imagery

Coalignment of LiDAR and hyperspectral imagery can be achieved by ground control points or by unsupervised image registration. Our NGF-Curv method adopts the latter approach

[38]. The true color composites of red, green, and blue (RGB) bands (640, 549, and 460 nm) of hyperspectral imagery were converted to greyscale images by MATLAB's built-in function `rgb2gray` and the greyscale image was used for the registration. LiDAR was converted to a digital surface model (DSM)—interpolating LiDAR first returns. The DSM was used for the registration. Let reference R and template T images be the DSM taken from LiDAR and the greyscale image obtained from the hyperspectral imagery, respectively. The LiDAR DSM image was used as the reference image because the spatial resolution of the LiDAR DSM image was more accurate than that of the hyperspectral imagery. Reference R and template T are modeled as functions defined on a finite 2-D grid Ω , mapping a point x on the grid to a real intensity value $R(x)$ and $T(x)$, respectively. The objective of the image registration is to find an optimal transformation mapping $u: \Omega \rightarrow \Omega$ that coaligned the template image to the reference image. The NGF-Curv method we used computes the transformation u as a minimizer of an energy that consists of a similarity term D and a regularization term S . That is, u is the solution of the following problem:

$$\min_u \left\{ \sum D[R(x), T(u(x))] + \alpha S(u) \right\}$$

where α is the regularization parameter which balances the similarity term and the regularization term. The similarity term D used is defined by

$$1 - \left[\left(\frac{\nabla T(u)}{\sqrt{|\nabla T(u)|^2 + \eta^2}} \right)^t \left(\frac{\nabla R}{\sqrt{|\nabla R|^2 + \eta^2}} \right) \right]^2$$

which is the so-called NGF distance measure, where $\eta > 0$ is an edge parameter which represents the level of the noise in the images and ∇^t is the transpose of the discrete gradient in 2-D. To impose smoothness features on the transformation u , we use the curvature in the regularization term S , i.e.,

$$S(u) = \frac{1}{2} \sum_{x \in \Omega} |\Delta u(x)|^2$$

where Δ is the discretized Laplace operator. For more details, we refer to [38] and references therein.

B. Feature Extraction

Extracting feature information from the hyperspectral imagery is a key step to map individual trees with species information. As the hyperspectral imagery contains 361 spectral bands (i.e., dimensionality is high), the meaningful features are hidden inside an enormous number of spectral bands. To extract the most meaningful features, a data pruning technique rPCA [41] is implemented in our workflow.

Let M be a $m \times n$ measurement matrix, where m is the number of spatial pixels of the hyperspectral imagery, n is the number of spectral bands of the hyperspectral imagery. Principal component analysis (PCA) finds a rank k matrix L from M , which may be corrupted by noise. It can be expressed by the following minimization problem:

$$\min_L \{ \|M - L\|_2\} \quad \text{s.t.} \quad \mathcal{R}(L) < k \quad (1)$$

where $\|\cdot\|_2$ is the ℓ_2 -norm, and $\mathcal{R}(\cdot)$ is the operator computing the rank of the given matrix. Problem (1) is solved explicitly by singular value decomposition. However, the PCA is sensitive to the magnitude of noise in the data [46], thus, it may not be suitable for extracting meaningful features from hyperspectral data. The rPCA method has been proposed to improve the robustness of the PCA method [41]. It aims to recover a low-rank matrix L from the noisy measurement matrix M , which is the hyperspectral imagery in our case, by removing a sparse outlier matrix S . The rPCA method can be represented by the following minimization problem:

$$\min_{L,S} \{\mathcal{R}(L) + \lambda\|S\|_0\} \quad \text{s.t.} \quad M = L + S \quad (2)$$

where $\|\cdot\|_0$ is the ℓ_0 -norm which counts the number of the nonzero entries therefore imposing sparsity property on S , and λ is a regularization parameter which balances the importance between the ranking operator and the sparsity regularization. This is a nonconvex optimization problem whose solution is in general NP-hard. To make the optimization problem (2) tractable, its convex relaxation using the nuclear norm $\|\cdot\|_*$ (sum of singular values) and the l_1 -norm (sum of the absolute values of all entries) were adopted instead of $\mathcal{R}(\cdot)$ and the l_0 -norm, respectively. This results in the following convex problem:

$$\min_{L,S} \{\|L\|_* + \lambda\|S\|_1\} \quad \text{s.t.} \quad M = L + S. \quad (3)$$

More details about rPCA can be found in [41] and references therein. Since (3) is a convex problem, it can be solved effectively by, for example, the alternating direction method for multipliers [47]. In fact, the parameter λ is fixed to $\frac{1}{\sqrt{m}}$. The validity of the parameter choice of λ is given by [41, Th. 1]. rPCA reduces the dimensionality of the hyperspectral imagery in a robust way. In addition, a user can prune the data further. The performance of rPCA will be discussed in Section V.

C. ITC Delineation

ITC delineation is performed by a normalized graphcut method constrained by prior knowledge directly on the 3-D LiDAR point clouds and the extracted features from Section III-B. See [48] and method MC–RC in [40] for a detailed explanation of the methodology.

Let \mathbf{G} be a graph containing a set of pairs, $\mathbf{G} = (\boldsymbol{\nu}, \epsilon)$, where $\boldsymbol{\nu}$ is the set of vertices and ϵ is the set of edges. Each edge $w(\nu_i, \nu_j) \in \epsilon$ corresponds to the nonnegative similarity weight w_{ij} between two vertices ν_i and ν_j . Such a graph is built using the LiDAR point clouds. The similarity weights depend on Euclidean distances between the LiDAR points as well as extracted features from hyperspectral imagery. The details of how to define the weights is given by Lee *et al.* [40].

Let \mathbf{W} be an $N \times N$ symmetric matrix with entries $\mathbf{W}(i,j) = w_{ij}$ given by the weights, \mathbf{D} be an $N \times N$ diagonal matrix with diagonal entries $d_i = \sum_j w_{ij}$, $\mathbf{1}$ be an $N \times 1$ all-ones vector, \mathbf{I} be a $C \times C$ identity matrix, and \mathbf{X} is the unknown labeling, which is an $N \times C$ matrix, where C is the number of clusters in the point cloud. The normalised cut seeks

an optimal labelling \mathbf{X} as the solution of

$$\begin{aligned} & \min_{\mathbf{X}} \text{tr}(\mathbf{X}^T \mathbf{D}^{-\frac{1}{2}} (\mathbf{D} - \mathbf{W}) \mathbf{D}^{-\frac{1}{2}} \mathbf{X}) \\ & \text{s.t.} \quad \mathbf{X}^T \mathbf{D}^{\frac{1}{2}} \mathbf{1} = \mathbf{0}, \quad \mathbf{X}^T \mathbf{X} = \mathbf{I} \end{aligned}$$

where $\text{tr}(\cdot)$ is the trace of a matrix.

In our algorithm, the original normalized cut is relaxed as a convex optimization problem and guided by prior information about the likely location of trees. It is not straightforward to incorporate prior knowledge in normalized graphcut, as the normalized cut finds optimal partitioning from the graph of the similarity weights. In our modified scheme, prior information is regarded as an additional constraint in the normalized graphcut approach. It minimizes the normalised cut energy as well as satisfying a correlation constraint with priors. The correlation term $\text{diag}(\mathbf{X}^T \mathbf{S}) = \kappa \text{diag}(\mathbf{I})$ incorporates a prior information matrix \mathbf{S} , which consists of the local maxima of the canopy height model (CHM) and their neighbor points. Here κ is a correlation coefficient. The CHM was obtained by subtracting bare-earth topography from the DSM. Our modified multiclass normalised graphcut can be written as follows:

$$\begin{aligned} & \min_{\mathbf{X}} \text{tr}(\mathbf{X}^T \mathbf{D}^{-\frac{1}{2}} (\mathbf{D} - \mathbf{W}) \mathbf{D}^{-\frac{1}{2}} \mathbf{X}) \\ & \text{s.t.} \quad \text{diag}(\mathbf{X}^T \mathbf{X}) = \text{diag}(\mathbf{I}), \quad \mathbf{X}^T \mathbf{D}^{\frac{1}{2}} \mathbf{1} = \mathbf{0} \\ & \quad \text{diag}(\mathbf{X}^T \mathbf{S}) = \kappa \text{diag}(\mathbf{I}). \end{aligned}$$

The locations of local maxima were computed by the toolbox for LiDAR data filtering and a standard forest analysis (TIFFS, Globalidar Ltd.) [30]. Although we used TIFFS for extracting priors, users could use any tree top searching algorithm to get priors. We refer to [40] for more details.

D. Species Classification

For the classification of the tree species we used the SVM method, that is a nonparametric supervised classifier, which has been showed to be superior to other classification strategies in several studies [23], [26], [35], [49], [50]. We applied SVM on the extracted features from Section III-B in order to classify species, initially at the pixel level.

For a training data set $\mathcal{T} = \{(x_1, y_1), \dots, (x_n, y_n)\}$ consisting of pairs of feature vectors $x_i \in \mathcal{F}$ (where $\mathcal{F} \subset \mathbb{R}^m$ is a m -dimensional feature space), and labels y_i (for example, the binary label $y_i \in \{-1, 1\}$ in the case of two species). Then, SVM finds a separating hyperplane $H := \{x \mid \langle w, \eta(x_i) \rangle - b = 0\}$ (where w is a normal vector to the hyperplane, b is the intercept and $\eta(x_i) : \mathcal{F} \rightarrow \bar{\mathcal{F}}$ is a nonlinear embedding that transforms the original feature space to a higher dimensional space). H has dimension depending on the number of species (labels) in y_i although typically the dimension is 1 (SVM for binary classification). In this study, we adopt the radial basis kernel $\exp(-\gamma \|x - x'\|_2^2)$ for η , where γ is the parameter for the radial basis. Therefore, the higher dimensional space $\bar{\mathcal{F}}$ is where the radial basis functions lives.

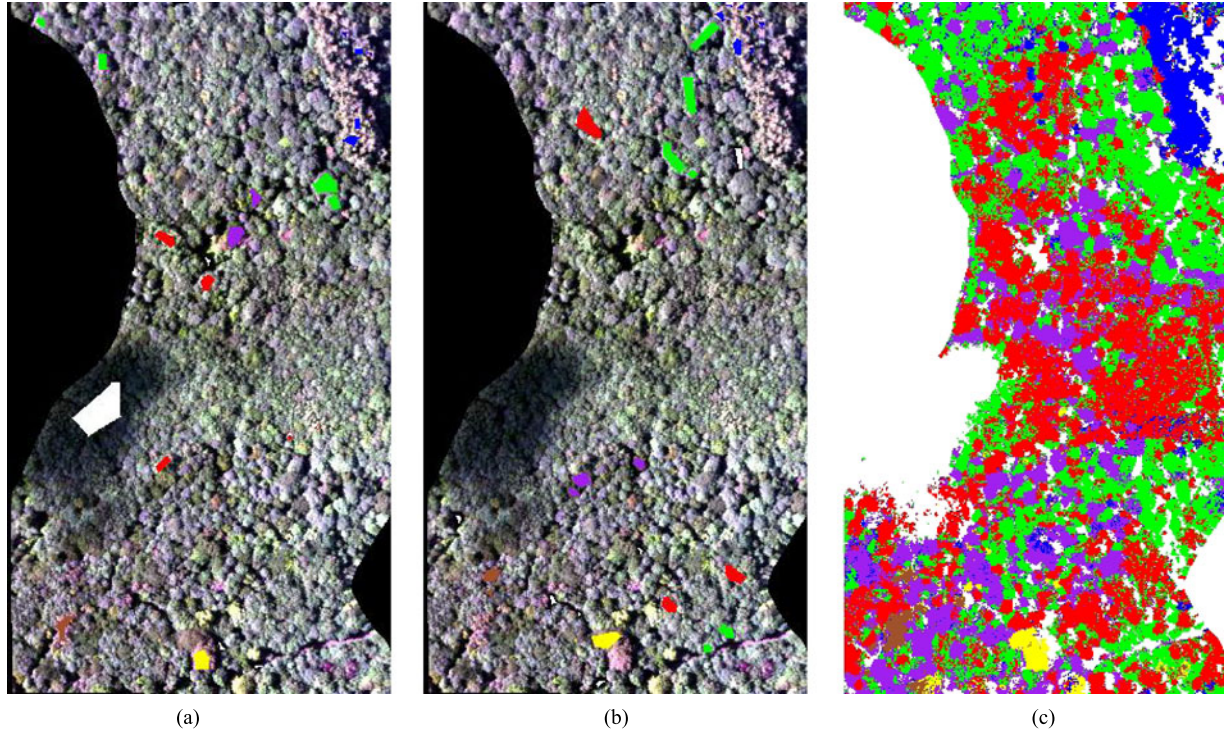


Fig. 3. Pixel-level species classification in Wytham Woods. The colored polygons in (a) and (b) represent training and test samples of each species overlaid over a false color representation of the hyperspectral imagery. The color map (c) shows the result of the pixel-level species classification by our proposed workflow. Colors indicate different species, i.e., blue = *Larix decidua*, green = *Acer pseudoplatanus*, red = *Fraxinus excelsior*, yellow = *Fagus sylvatica*, purple = *Quercus robur*, brown = *Betula* spp., and white = shaded pixels.

The hyperplane H is then obtained by minimizing the following model:

$$\begin{aligned} \min_{w,b,\xi} & \|w\|_2^2 + C \sum_{i=1}^n \xi_i \\ \text{s.t. } & y_i \cdot (\langle w, \eta(x_i) \rangle - b) \geq 1 - \xi_i \\ & \xi_i \geq 0 \end{aligned}$$

where C is a regularization parameter and $\xi_i = \max(0, 1 - y_i \cdot \langle w, \eta(x_i) \rangle - b)$ is called a slack variable, which takes into account nonseparable data.

SVM is an intrinsically binary classifier, but it can be extended to multiclass problems by following two different strategies: one-against-one and one-against-all. In this study, we use the one-against-all rule, which solves K -binary problems instead of solving a K -class problem. We refer to [42] and references therein for an excellent introduction to SVM. A library for SVM for MATLAB was used to solve the multiclass SVM problem [42]. The optimal parameters for SVM classification were found by trial and error. The regularization parameter C was fixed to 100, and the parameter γ was set to 0.5 for all experiments in Section IV.

Fig. 3(a) and (b) shows the location of the training and test samples used for the pixel-level tree species classification evaluation. Table II shows the number of pixels for each species used as training and test samples. The training and test samples of the hyperspectral imagery were extracted from manually delineated ITC by means of visual inspection and field data. We

TABLE II
NUMBER OF PIXELS FOR EACH SPECIES OF THE TRAINING AND TEST SAMPLES
FOR TREE SPECIES CLASSIFICATION

Species	Training samples	Test samples
<i>Fraxinus excelsior</i>	226	410
<i>Acer pseudoplatanus</i>	304	431
<i>Larix decidua</i>	126	129
<i>Quercus robur</i>	178	149
<i>Fagus sylvatica</i>	139	199
<i>Betula</i> spp.	93	93
Shade	844	126
Overall (No. of pixels)	1910	1537

considered only trees with height above 18 m. It makes sense to mask out understory trees since spectral signatures captured from the hyperspectral imagery mainly originate from canopy leaves. The ITC-level tree species classification map is obtained by extracting the pixel-level map for each ITC and applying a majority voting rule [9], [35] to decide the species for each crown (ITC level). Therefore, the most frequent species class inside of each ITC represents the species of ITCs.

E. Validation

The tree species classification was evaluated at both pixel- and ITC-level. The confusion matrix and reliability scores were used to evaluate the accuracy of species classification. Producer's, user's, and overall accuracies were computed starting from the confusion matrix. In addition, Cohen's kappa, quantity, and

TABLE III
SPECIES CLASSIFICATION RESULTS OBTAINED BY THE ITSC METHOD BASED ON PCA

Species	Ground truth							Total	Producer's accuracy (%)
	Fraxinus excelsior	Acer pseudoplatanus	Larix decidua	Quercus robur	Fagus sylvatica	Betula spp.	Shade		
Classification results	<i>Fraxinus excelsior</i>	377	24	1	7	0	0	410	92.0
	<i>Acer pseudoplatanus</i>	48	356	3	24	0	0	431	82.6
	<i>Larix decidua</i>	0	2	125	0	0	2	129	96.9
	<i>Quercus robur</i>	0	0	5	143	0	1	149	96.0
	<i>Fagus sylvatica</i>	0	7	18	25	139	8	199	70.0
	<i>Betula</i> spp.	3	6	1	22	4	57	93	61.2
	Shade	0	0	0	4	0	0	122	96.8
Total		428	395	153	225	143	68	125	1537
User's accuracy (&)		88.1	90.1	81.7	63.6	97.2	83.8	97.6	85.8

Kappa accuracy = 0.825, quantity disagreement = 0.077, allocation disagreement = 0.065.

TABLE IV
SPECIES CLASSIFICATION RESULTS OBTAINED BY THE ITSC-R METHOD BASED ON rPCA

Species	Ground truth							Total	Producer's accuracy(%)
	Fraxinus excelsior	Acer pseudoplatanus	Larix decidua	Quercus robur	Fagus sylvatica	Betula spp.	Shade		
Classification results	<i>Fraxinus excelsior</i>	377	16	0	13	0	0	4	92.0
	<i>Acer pseudoplatanus</i>	11	390	2	28	0	0	1	90.5
	<i>Larix decidua</i>	0	0	129	0	0	0	129	100
	<i>Quercus robur</i>	0	0	0	148	1	0	0	99.3
	<i>Fagus sylvatica</i>	0	0	3	10	181	1	199	91.0
	<i>Betula</i> spp.	0	1	12	1	10	69	0	74.2
	Shade	0	0	8	2	0	0	116	92.1
Total		388	407	137	219	192	70	124	1537
User's accuracy (&)		97.2	95.8	94.1	67.6	94.3	98.6	93.6	91.7

Kappa accuracy = 0.898, quantity disagreement = 0.051, allocation disagreement = 0.032.

TABLE V
SPECIES CLASSIFICATION RESULTS AT ITC LEVEL

Species	Ground truth							Total	Producer's accuracy (%)
	Fraxinus excelsior	Acer pseudoplatanus	Larix decidua	Quercus robur	Fagus sylvatica	Betula spp.	Other species		
Classification results	<i>Fraxinus excelsior</i>	146	38	4	36	0	0	224	65.2
	<i>Acer pseudoplatanus</i>	82	205	3	50	0	1	341	60.2
	<i>Larix decidua</i>	5	2	4	2	0	0	13	30.8
	<i>Quercus robur</i>	4	19	0	53	0	1	77	68.8
	<i>Fagus sylvatica</i>	1	0	0	0	3	0	4	75.0
	<i>Betula</i> spp.	2	0	0	1	0	6	9	66.7
	Other species	9	5	1	0	0	0	15	0
Total		249	269	11	143	3	8	0	677
User's accuracy (&)		58.6	76.2	37.1	36.4	100	75.0	0	61.1

Kappa accuracy = 0.410, quantity disagreement = 0.133, allocation disagreement = 0.256.

allocation disagreement were computed for the reliability of the classification results (see Tables III–V) [51].

IV. RESULTS

This section presents the experimental results of our individual tree species classification approach. We present the results

of using both PCA and rPCA in the feature extraction step of the workflow to explore whether rPCA delivers more accurate results over the traditional approach. We refer to workflows using PCA and rPCA in the feature extraction step as the ITSC and ITSC-R methods, respectively. For the results shown here, the feature extraction was applied only to the hyperspectral imagery.

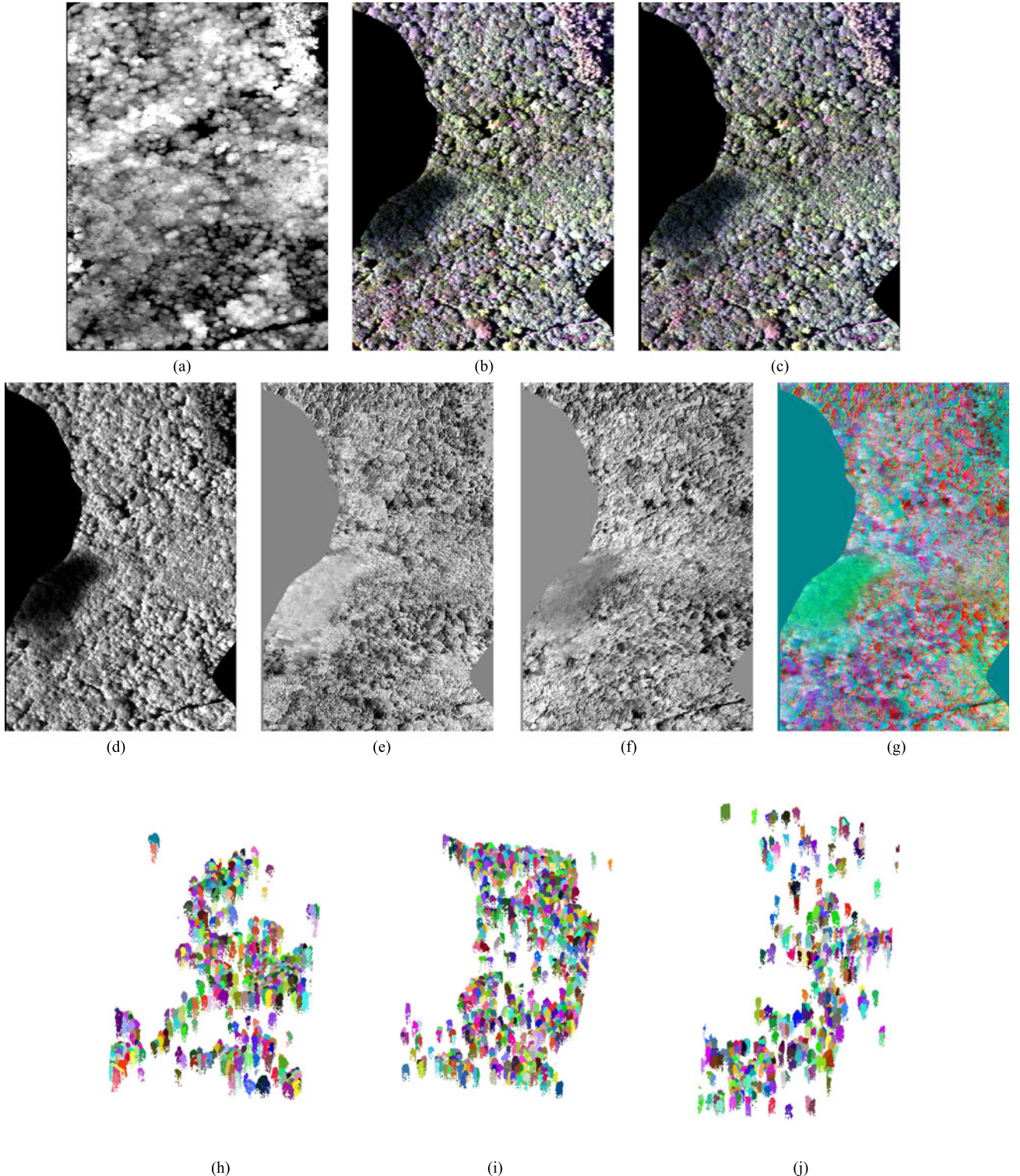


Fig. 4. Results of the images coalignment, feature reduction and ITC delineation in our workflow. The first row shows the image registration between LiDAR DSM (a) and RGB true color hyperspectral imagery (b) and the coaligned hyperspectral imagery in RGB true color (c). The second row shows the first three principal components (d)–(g). The third row shows examples of the MC-RC segmentation viewed obliquely (h)–(j) and different colors represent ITCs.

Fig. 4 summarizes the results of steps A, B, and C of the workflow: Fig. 4(a) and (b) shows the LiDAR (CHM) and a false color representation of the hyperspectral imagery, and Fig. 4(c) shows the coalignment result using the NGF-Curv registration method [38]. Since the initial alignment between LiDAR and

hyperspectral imagery was excellent, any errors were too small to be apparent visually in our dataset. Fig. 4(d)–(g) shows the first three principal components obtained by the rPCA method and their RGB color composite. In our workflow, the first 20 principal components were used to delineate ITCs along with

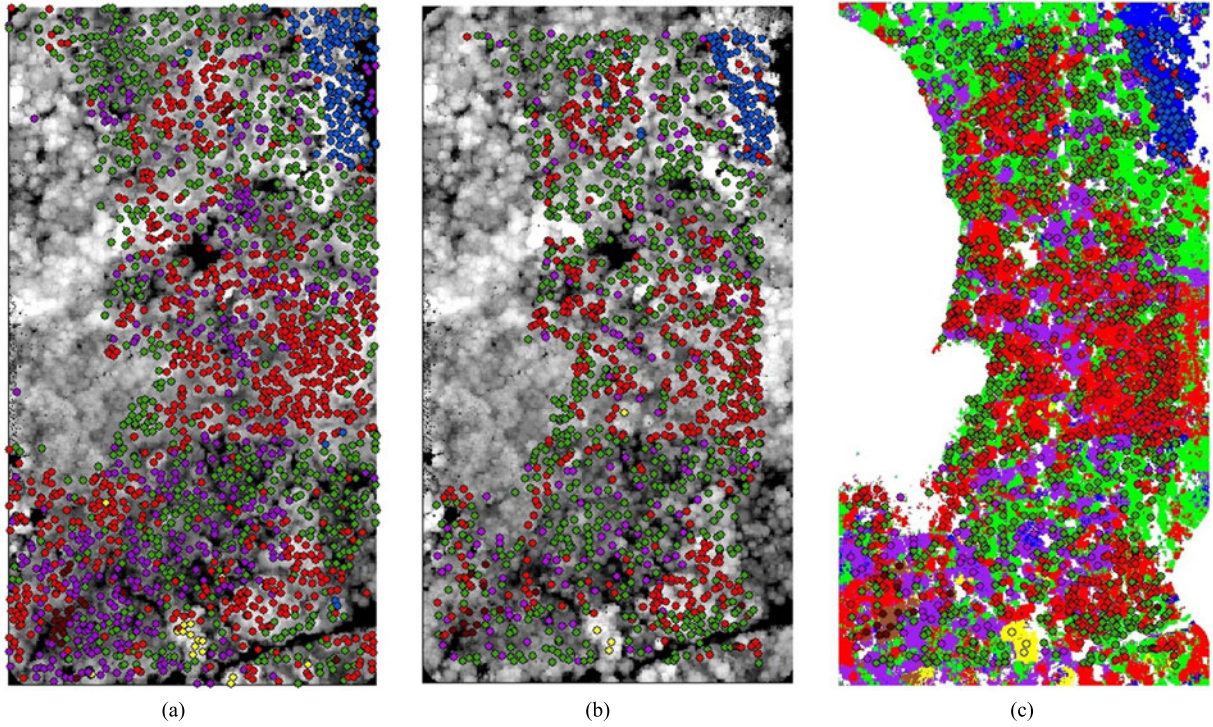


Fig. 5. Mapping individual tree species at ITC level and ground truth. The background images in (a)–(c) are DSM. The colored map in (c) is pixel-level species classification, where each color indicates different species. The circles in colors represent ITCs of different species. Blue = *Larix decidua*, green = *Acer pseudoplatanus*, red = *Fraxinus excelsior*, yellow = *Fagus sylvatica*, purple = *Quercus robur*, and brown = *Betula* spp.

LiDAR using the MC–RC [40], and classify species at the pixel- and ITC-levels. Fig. 4(h)–(j) shows the ITC delineation results.

A. Pixel-Level Tree Species Classification

Fig. 3(c) shows the species classification results over the 18-ha field plot in Wytham Woods. The results for the test samples, presented in Tables III and IV, show the overall accuracy of the ITSC-R method at pixel level was 91.7% while that of the ITSC method was 85.8%. In overall, the ITSC-R method performed better than the ITSC method.

Regarding the individual species, for *Fraxinus excelsior*, the producer's accuracy was 92.0 % for both ITSC-R and ITSC methods, but the ITSC-R method performed better with respect to the user's accuracy. The ITSC-R method outperformed the ITSC method for producer's accuracy and user's accuracy of *Acer pseudoplatanus*. The ITSC-R method showed better performance with respect to producer's accuracy for *Quercus robur*, while user's accuracies were poor for both ITSC-R and ITSC methods. The confusion matrices of both ITSC-R and ITSC methods (see Tables IV and III) show that *Fraxinus excelsior* was confused mainly with *Acer pseudoplatanus* and *Quercus robur*. *Acer pseudoplatanus* was confused with *Fraxinus excelsior* and *Quercus robur*. This is the reason for the low user's accuracy of *Quercus robur*. It makes sense as the ground truth data in Fig. 5 clearly shows that these three species are dominant in the study site and often are mixed. *Larix decidua* was dominant at the north-east edge of the study site, and both ITSC-R and ITSC methods successfully classified all the test samples of this species. However, *Larix decidua* was one of the major confusing

factor for *Fagus sylvatica* pixels, so the user's accuracy of *Larix decidua* was poor for the ITSC method. The producer's accuracy of *Fagus sylvatica* was only 70.0% for the ITSC method as it was confused with *Quercus robur* and *Larix decidua* pixels. For the ITSC-R method, the producer's and user's accuracies of *Fagus sylvatica* were 91.0% and 94.3%, respectively. The producer's accuracy of *Betula* species was only 61.2% for the ITSC method, while the ITSC-R method achieved 74.2% producer's accuracy. With respect to the user's accuracy of *Betula* species, the ITSC-R method achieved 98.6%, while the ITSC method only had 83.8%.

B. ITC-Level Species Classification—Mapping Individual Trees

Species classification at ITC level was validated using software specifically designed for validating tree segmentation, called the NewFor software [52], [53]. This software uses tree heights and tree locations to find the best matching candidates between the ground truth and the segmented tree crowns. The software, therefore, is sensitive to the initial positioning of the ground truth. To alleviate this problem, we also included two figures to evaluate species classification at ITC level. Fig. 5 shows both the pixel- and ITC-level species classification results along with the ground truth information. Fig. 6 shows the map of ITCs of each species using the MC–RC algorithm and the ground truth data. These two figures will be used to compare the patterns of species distribution across the study site.

In total, 1687 ITCs were delineated by MC–RC algorithm. However, the NEWFOR algorithm used to test delineation

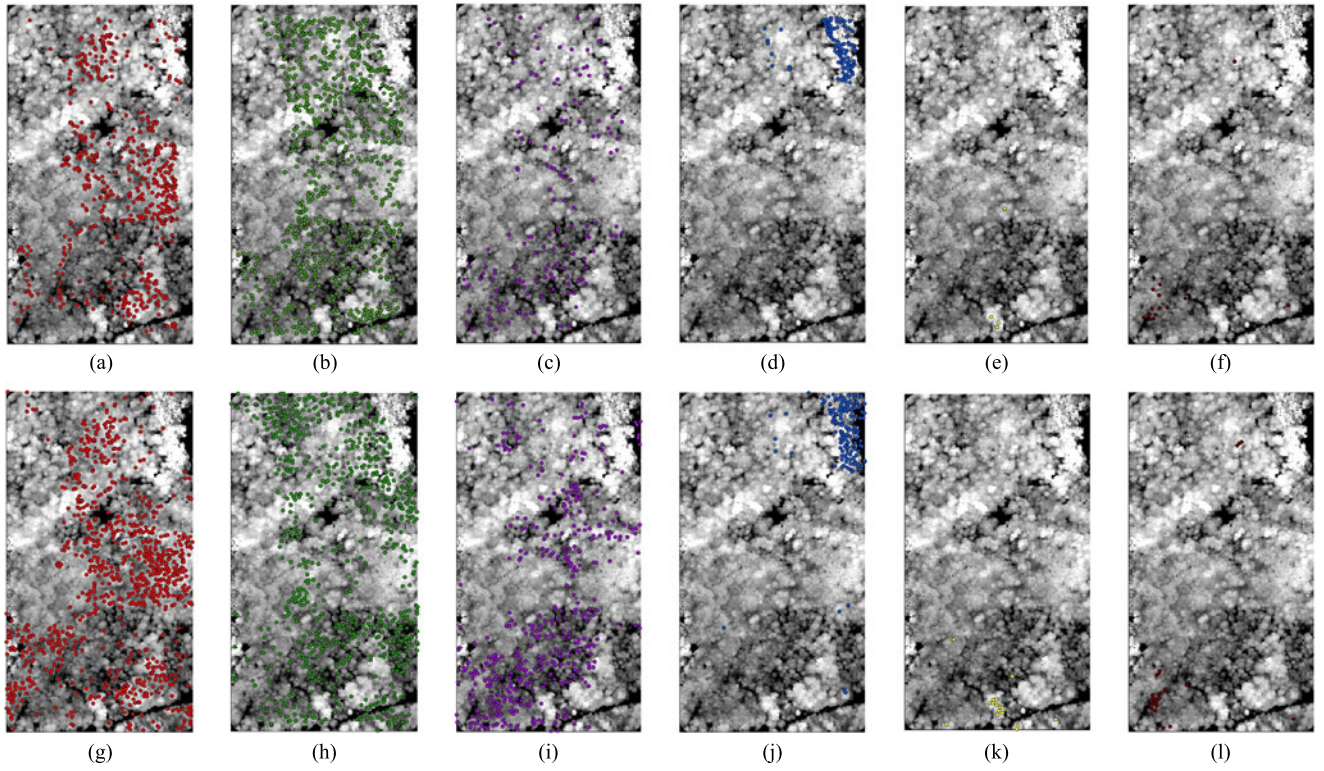


Fig. 6. Mapping each species at ITC level and the ground truth. Each circle represents a single ITC. The first row shows the ground truths canopy trees over 18 m. The second row shows the results of ITC-level species classification. Colors indicate different species, i.e., blue = *Larix decidua*, green = *Acer pseudoplatanus*, red = *Fraxinus excelsior*, yellow = *Fagus sylvatica*, purple = *Quercus robur*, and brown = *Betula* spp.

accuracy indicated that 683 ITCs were correctly delineated. The number of false positives generated by our algorithm were 1004, while 1002 ground truth trees were missing. The performance of ITC-level species classification was examined only for the 683 ITCs, which were corrected delineated by the validation software. However, the visual analysis of Fig. 6 showed that the validation software does not accurately describe the performance of the ITC-level species classification. For example, *Larix decidua* is dominant at the north-east edge of the study site. Since *Larix decidua* is a coniferous tree, it is relatively easy to delineate its crowns accurately. However, the validation results and Table V show that almost 87% *Larix decidua* trees were omitted according to the validation results. In Fig. 6(d) and (j), the patterns of *Larix decidua* from segmented ITCs and ground truth field data were very similar. This is mainly because the software is sensitive to the accuracy of tree coordinates in the ground data. Horizontal and vertical distances within 5 m between ground and segmented trees are considered to be matched. Since ground truth dataset had positioning errors of around 10 m, large commission and omission errors arose.

Table V shows the confusion matrix at ITC level, which considers only correctly assigned ITCs. The overall accuracy was only 61.1%, which was lower than that at pixel level. *Fraxinus excelsior* classification indicates that both producer's and user's accuracies were poor, while visual comparison of ground truth and species map in Figs. 5 and 6(a) and (g) shows that species distribution patterns of ground truth and species map had a good agreement. The ITC-level classification of *Acer pseudoplatanus*

was 65.2% and 58.6% with respect to producer's and user's accuracies. Visual inspection of Fig. (b) and (h) suggested that ITC-level mapping of *Acer pseudoplatanus* agreed well with the ground truth data. *Larix decidua* was excluded from the validation as the ITC-level detection was unrealistic, but visual comparison implies that species distribution of pixel- and ITC-level were well agreed with the ground truth data. *Quercus robur* had a good producer's accuracy, while its user's accuracy was only 36.1%. This was in accordance with the pixel-level classification of *Quercus robur*. In particular, visual analysis of the ITC delineation suggests that *Quercus robur* was oversegmented [see Fig. 6(c) and (i)]. This might be because some branches were extracted as different local maxima, so the segmentation algorithm oversegmented the oak trees. The accuracy of *Fagus sylvatica* had high producer's accuracy and user's accuracy. Oversegmentation was observed in visual inspection. This was partly because we only selected canopy trees over 18 m, so some canopy trees were omitted. In addition, some branches of *Fagus sylvatica* were identified as local maxima, thereby causing commission errors. The accuracy of *Betula* spp. was relatively high compared to other species. *Betula* spp. are located in a small area at southwest edge of the study site, so they can be mapped more easily [see Fig. 6(f) and (l)].

V. DISCUSSION

The rPCA feature reduction technique provides a rich information for distinguishing species with far fewer dimensions than

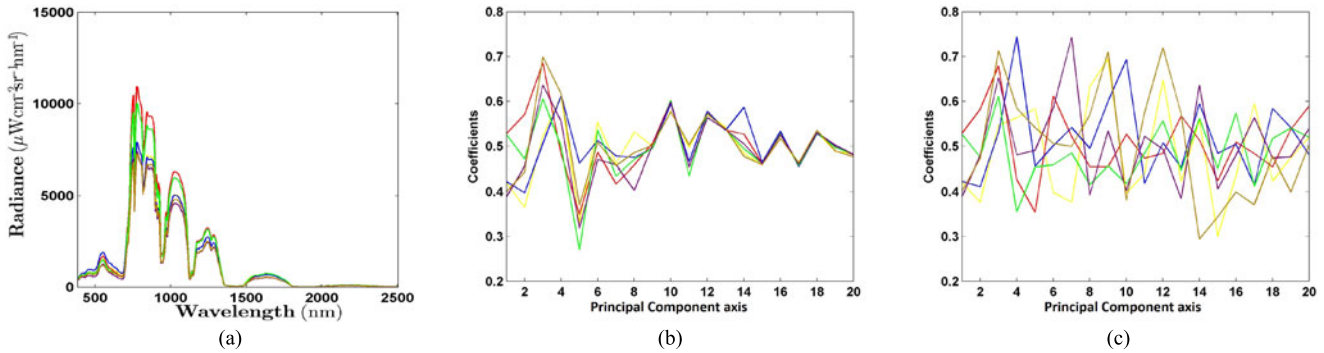


Fig. 7. Spectral signatures and principal component coefficients of six dominant canopy tree species. Panel (a) shows spectral signatures of species, (b) and (c) are the mean coefficients of PCA and rPCA of species, respectively. Colors in (a)–(c) represent different species, i.e., blue = *Larix decidua*, green = *Acer pseudoplatanus*, red = *Fraxinus excelsior*, yellow = *Fagus sylvatica*, purple = *Quercus robur*, and brown = *Betula spp.*

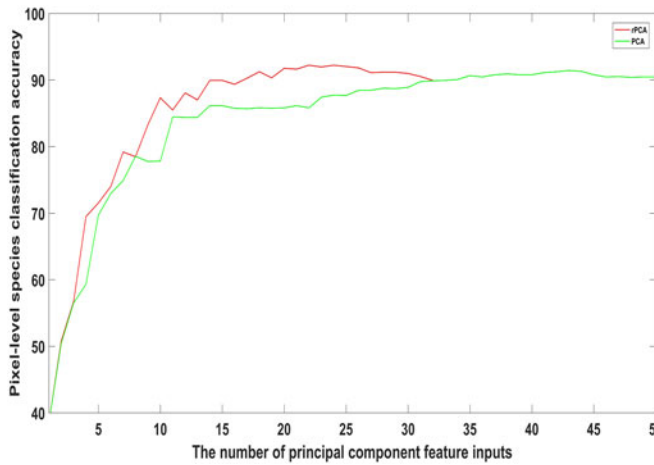


Fig. 8. The pixel-level classification accuracy with respect to the number of principal component feature inputs.

the original hyperspectral datasets. Fig. 7(a) shows that spectral radiance of *Fraxinus excelsior* and *Acer pseudoplatanus* is similar to each other and have greater radiance values than other species. The first few principal components of PCA and rPCA reveal the same pattern, with *Fraxinus excelsior* and *Acer pseudoplatanus* having higher coefficients than the other species [see Fig. 7(b) and (c)]. It is important to note that PCA coefficients of different species tend to be similar for higher axes, so have little value in guiding species classification. In contrast, the coefficients from higher rPCA bands are very different among species, so provide meaningful signals with which to identify species. How to select the best number of principal component feature to give in input to the classifier is another challenging question. In our case, rPCA reduced the dimensionality of the data from 361 to 32. After visually examining the noise in each PC axis, we selected the first 20 PCs. The sensitivity analysis of the pixel-level classification accuracy with respect to different numbers of PC feature inputs is presented in Fig. 8. In overall, the pixel-level classification using rPCA showed at least the same or better accuracy. The best pixel-level classification accuracy using rPCA was achieved when we considered the

first 22 PCs (92.19%). Then, it decreased slightly. On the other hand, PCA achieved the best classification accuracy with the first 43 PCs (91.41%).

In this study, pixel-level species classification was conducted using only hyperspectral imagery, because our emphasis was on improving species classification from hyperspectral imagery using rPCA technique. Many studies have reported that using LiDAR features can improve species classification, since LiDAR is not influenced by illumination artifacts [23], [26]–[28]. LiDAR intensity may provide more detailed radiometric information for guiding species classification, however, in our acquisition LiDAR intensity was controlled in nonlinear way by automatic gain control, thus, it was not possible to calibrate the intensity and to use it for species classification. In addition, illumination information is important for finding shaded pixels in our method, so the improvement by additional features from LiDAR may not be significant. Investigating the role of LiDAR derived metrics on species classification could provide better understanding of species classification [22], but this is the beyond of the scope of this paper.

Species classification at pixel level is strongly influenced by illumination effects [14], [31], [35], [54]. Species classification using only sunlit pixels produce better results than considering all pixels [14]. Thus, a shadow removal step may be seen as a prerequisite. Shadow removal can be done by manual selection [14], [29], ray tracing simulation with LiDAR derived DSM [54], ITC information from LiDAR [31], or normalised difference vegetation index filtering [34]. In this study, shaded pixels were included as additional class for learning (see Fig. 3), such that shaded pixels were detected during the pixel-level species classification process as previously suggested by Dalponte *et al.* [26]. This strategy is particularly useful as we can detect shaded pixels without particularly processing the shaded area. The producer's and user's accuracies of shaded pixel detection were high in both ITSC and ITSC-R methods. It is well known that the first principal component is mainly related with illumination effects [55], which may be linked with high accuracy of shaded pixel detection of our method. Although Tochon *et al.* [55] report that the first component of PCA is

not useful for ITC delineation, it can, at least, be used for more accurate pixel-level species classification by detecting shaded pixels.

The size of training dataset may affect the species classification result. In this paper, approximately 1–7 crowns per species were used to classify all species and shaded pixels. Baldeck and Asner [56] showed that the sensitivity of species classification on sample size is dependent on the number of species and spectral separability of each species. In that study, the optimal number of tree crowns for species classification in a savanna woodland was 10 trees for two species and 19 trees for 11 species; i.e., they used more tree samples. This difference might be related with the types of forest. We tested our workflow in a temperate forest, while their research was conducted in a savanna woodland. We also used rPCA to reduce 361 spectral bands to 20 principal components, so direct comparison of these papers may not work. Moreover, airborne hyperspectral imagery used in this paper contained spectral signals spanning from the visible to SWIR (400–2500 nm) wavelength region, while, the spectrometer used by Pontius Jr. and Millones [56] had spectral coverage from visible and NIR wavelength region (400–1000 nm). The SWIR region may give more spectral separability, so it could reduce the sample size needed for species classification. Finding an optimal size of training samples in our test site requires further analysis, but we leave it for future work.

VI. CONCLUSION AND OUTLOOK

This study investigated the possibility of species mapping using airborne remote sensing datasets. Although several algorithms have been suggested for species mapping over various types of forest, their system architectures assumed coalignment of LiDAR and hyperspectral imagery, so it was difficult to apply directly. In addition, their methodologies for delineating ITC were mostly based on DSMs rather than LiDAR point cloud, so both forest and ITC parameter estimation were relatively inaccurate. We introduced 3-D tree delineation algorithm MC–RC in our workflow, so forest analysis at species level, such as total biomass estimation of each canopy species, can be conducted more accurately. Our workflow has provided a general framework to fuse multisensor imagery and demonstrated its efficiency in a mixed temperate forest. Our pixel-level species classification method showed that 89% of pixels were correctly assigned overall. The overall accuracy of ITC-level tree species classification was 65.8%. The low accuracy at the ITC-level classification might be related to inaccurate geopositioning of the ground truth dataset because visual analysis showed that species distribution patterns agreed well with ground truth. Further study is required to evaluate our method with accurately georeferenced ground truth data. Nonetheless, this study shows the potential of rPCA and machine learning approaches to distinguish species using hyperspectral imagery.

ACKNOWLEDGMENT

The authors would like to thank NERC-ARSF for collecting and preprocessing the data used in this research project [RG13/08/175b].

REFERENCES

- [1] G. Asner, D. Knapp, A. Balaji, and G. Páez-Acosta, "Automated mapping of tropical deforestation and forest degradation: Claslite," *J. Appl. Remote Sens.*, vol. 3, no. 1, pp. 033543–033543, 2009.
- [2] R. Houghton, K. Lawrence, J. Hackler, and S. Brown, "The spatial distribution of forest biomass in the brazilian amazon: A comparison of estimates," *Global Change Biol.*, vol. 7, no. 7, pp. 731–746, 2001.
- [3] Z. A. Latif, I. Zamri, and H. Omar, "Determination of tree species using worldview-2 data," in *Proc. IEEE 8th Int. Colloq. Signal Process. Appl.*, 2012, pp. 383–387.
- [4] M. Immitzer, C. Atzberger, and T. Koukal, "Tree species classification with random forest using very high spatial resolution 8-band worldview-2 satellite data," *Remote Sens.*, vol. 4, no. 9, pp. 2661–2693, 2012.
- [5] K. Y. Peerbhoy, O. Mutanga, and R. Ismail, "Investigating the capability of few strategically placed worldview-2 multispectral bands to discriminate forest species in KwaZulu-Natal, South Africa," *IEEE J. Sel. Topics Appl. Earth Observ. Remote Sens.*, vol. 7, no. 1, pp. 307–316, Jan. 2014.
- [6] G. Omer, O. Mutanga, E. M. Abdel-Rahman, and E. Adam, "Performance of support vector machines and artificial neural network for mapping endangered tree species using worldview-2 data in dukuduku forest, south africa," *IEEE J. Sel. Topics Appl. Earth Observ. Remote Sens.*, vol. 8, no. 10, Oct. 2015.
- [7] G. P. Asner, R. E. Martin, A. J. Ford, D. J. Metcalfe, and M. J. Liddell, "Leaf chemical and spectral diversity in australian tropical forests," *Ecological Appl.*, vol. 19, no. 1, pp. 236–253, 2009.
- [8] J.-B. Féret and G. P. Asner, "Spectroscopic classification of tropical forest species using radiative transfer modeling," *Remote Sens. Environ.*, vol. 115, no. 9, pp. 2415–2422, 2011.
- [9] J.-B. Féret and G. P. Asner, "Tree species discrimination in tropical forests using airborne imaging spectroscopy," *IEEE Trans. Geosci. Remote Sens.*, vol. 51, no. 1, pp. 73–84, Jan. 2013.
- [10] G. P. Asner, "Biophysical and biochemical sources of variability in canopy reflectance," *Remote Sens. Environ.*, vol. 64, no. 3, pp. 234–253, 1998.
- [11] M. Cochrane, "Using vegetation reflectance variability for species level classification of hyperspectral data," *Int. J. Remote Sens.*, vol. 21, no. 10, pp. 2075–2087, 2000.
- [12] K. L. Castro-Esau, G. A. Sánchez-Azofeifa, B. Rivard, S. J. Wright, and M. Quesada, "Variability in leaf optical properties of mesoamerican trees and the potential for species classification," *Amer. J. Botany*, vol. 93, no. 4, pp. 517–530, 2006.
- [13] G. Asner *et al.*, "Carnegie airborne observatory: In-flight fusion of hyperspectral imaging and waveform light detection and ranging for three-dimensional studies of ecosystems," *J. Appl. Remote Sens.*, vol. 1, no. 1, pp. 0135 36–0135 36, 2007.
- [14] M. L. Clark, D. A. Roberts, and D. B. Clark, "Hyperspectral discrimination of tropical rain forest tree species at leaf to crown scales," *Remote Sens. Environ.*, vol. 96, no. 3, pp. 375–398, 2005.
- [15] J. Zhang, B. Rivard, A. Sánchez-Azofeifa, and K. Castro-Esau, "Intra- and inter-class spectral variability of tropical tree species at La Selva, Costa Rica: Implications for species identification using hydice imagery," *Remote Sens. Environ.*, vol. 105, no. 2, pp. 129–141, 2006.
- [16] M. A. Cho, P. Debba, R. Mathieu, L. Naidoo, J. Van Aardt, and G. P. Asner, "Improving discrimination of savanna tree species through a multiple-endmember spectral angle mapper approach: Canopy-level analysis," *IEEE Trans. Geosci. Remote Sens.*, vol. 48, no. 11, pp. 4133–4142, Nov. 2010.
- [17] C. A. Baldeck and G. P. Asner, "Single-species detection with airborne imaging spectroscopy data: A comparison of support vector techniques," *IEEE J. Sel. Topics Appl. Earth Observ. Remote Sens.*, vol. 8, no. 6, pp. 2501–2512, Jun. 2015.
- [18] M. Dalponte, L. Bruzzone, L. Vescovo, and D. Gianelle, "The role of spectral resolution and classifier complexity in the analysis of hyperspectral images of forest areas," *Remote Sens. Environ.*, vol. 113, no. 11, pp. 2345–2355, 2009.
- [19] K. M. Dahlin, G. P. Asner, and C. B. Field, "Environmental and community controls on plant canopy chemistry in a mediterranean-type ecosystem," *Proc. Natl. Acad. Sci. USA*, vol. 110, no. 17, pp. 6895–6900, 2013.
- [20] N. Goodwin, R. Turner, and R. Merton, "Classifying eucalyptus forests with high spatial and spectral resolution imagery: An investigation of individual species and vegetation communities," *Aust. J. Botany*, vol. 53, no. 4, pp. 337–345, 2005.
- [21] R. Hill, A. Wilson, M. George, and S. Hinsley, "Mapping tree species in temperate deciduous woodland using time-series multi-spectral data," *Appl. Vegetation Sci.*, vol. 13, no. 1, pp. 86–99, 2010.

- [22] T. Matsuki, N. Yokoya, and A. Iwasaki, "Hyperspectral tree species classification of Japanese complex mixed forest with the aid of lidar data," *IEEE J. Sel. Topics Appl. Earth Observ. Remote Sens.*, vol. 8, no. 5, pp. 2177–2187, May 2015.
- [23] M. Dalponte, H. O. Orka, T. Gobakken, D. Ganelle, and E. Næsset, "Tree species classification in boreal forests with hyperspectral data," *IEEE Trans. Geosci. Remote Sens.*, vol. 51, no. 5, pp. 2632–2645, May 2013.
- [24] M. Dalponte, L. T. Ene, H. O. Orka, T. Gobakken, and E. Næsset, "Unsupervised selection of training samples for tree species classification using hyperspectral data," *IEEE J. Sel. Topics Appl. Earth Observ. Remote Sens.*, vol. 7, no. 8, pp. 3560–3569, Aug. 2014.
- [25] M. Colgan, C. B. adn J. Féret, and G. Asner, "Mapping savanna tree species at ecosystem scales using support vector machine classification and BRDF correction on airborne hyperspectral and LiDAR data," *Remote Sens.*, vol. 4, no. 11, pp. 3462–3480, 2012.
- [26] M. Dalponte, L. Bruzzone, and D. Ganelle, "Fusion of hyperspectral and LiDAR remote sensing data for classification of complex forest areas," *IEEE Trans. Geosci. Remote Sens.*, vol. 46, no. 5, pp. 1416–1427, May 2008.
- [27] T. G. Jones, N. C. Coops, and T. Sharma, "Assessing the utility of airborne hyperspectral and LiDAR data for species distribution mapping in the coastal pacific northwest, Canada," *Remote Sens. Environ.*, vol. 114, no. 12, pp. 2841–2852, 2010.
- [28] M. Dalponte, L. Bruzzone, and D. Ganelle, "Tree species classification in the southern alps based on the fusion of very high geometrical resolution multispectral/hyperspectral images and LiDAR data," *Remote Sens. Environ.*, vol. 123, pp. 258–270, 2012.
- [29] A. Ghosh, F. E. Fassnacht, P. Joshi, and B. Koch, "A framework for mapping tree species combining hyperspectral and LiDAR data: Role of selected classifiers and sensor across three spatial scales," *Int. J. Appl. Earth Observ. Geoinform.*, vol. 26, pp. 49–63, 2014.
- [30] Q. Chen, D. Baldocchi, P. Gong, and M. Kelly, "Isolating individual trees in a savanna woodland using small footprint LiDAR data," *Photogramm. Eng. Remote Sens.*, vol. 72, no. 8, pp. 923–932, 2006.
- [31] J. Heinzel and B. Koch, "Investigating multiple data sources for tree species classification in temperate forest and use for single tree delineation," *Int. J. Appl. Earth Observ. Geoinform.*, vol. 18, pp. 101–110, 2012.
- [32] C. Zhang and F. Qiu, "Mapping individual tree species in an urban forest using airborne LiDAR data and hyperspectral imagery," *Photogramm. Eng. Remote Sensing*, vol. 78, no. 10, pp. 1079–1087, 2012.
- [33] M. Voss and R. Sugumaran, "Seasonal effect on tree species classification in an urban environment using hyperspectral data, LiDAR, and an object-oriented approach," *Sensors*, vol. 8, no. 5, pp. 3020–3036, 2008.
- [34] M. Alonzo, B. Bookhagen, and D. A. Roberts, "Urban tree species mapping using hyperspectral and LiDAR data fusion," *Remote Sens. Environ.*, vol. 148, pp. 70–83, 2014.
- [35] M. Dalponte, H. O. Ørka, L. T. Ene, T. Gobakken, and E. Næsset, "Tree crown delineation and tree species classification in boreal forests using hyperspectral and ALS data," *Remote Sens. Environ.*, vol. 140, pp. 306–317, 2014.
- [36] C. Iovan, D. Boldo, and M. Cord, "Detection, characterization, and modeling vegetation in urban areas from high-resolution aerial imagery," *IEEE J. Sel. Topics Appl. Earth Observ. Remote Sens.*, vol. 1, no. 3, pp. 206–213, Sep. 2008.
- [37] R. Dinulis, G. Erins, A. Lorencs, I. Mednieks, and J. Sinica-Sinavskis, "Tree species identification in mixed baltic forest using LiDAR and multispectral data," *IEEE J. Sel. Topics Appl. Earth Observ. Remote Sens.*, vol. 5, no. 2, pp. 594–603, Apr. 2012.
- [38] J. Lee, X. Cai, C.-B. Schölieb, and D. Coomes, "Nonparametric image registration of airborne LiDAR, hyperspectral and photographic imagery of wooded landscapes," *IEEE Trans. Geosci. Remote Sens.*, to be published.
- [39] A. Persson, J. Holmgren, and U. Söderman, "Detecting and measuring individual trees using an airborne laser scanner," *Photogramm. Eng. Remote Sens.*, vol. 68, no. 9, pp. 925–932, 2002.
- [40] J. Lee, X. Cai, J. Lellmann, C.-B. Schölieb, and D. Coomes, "3D individual tree segmentation from fully integrated LiDAR, hyperspectral imagery and aerial photographs," DAMTP, Cambridge, U.K., Tech. Rep., 2015.
- [41] E. J. Candès, X. Li, Y. Ma, and J. Wright, "Robust principal component analysis?," *J. ACM*, vol. 58, no. 3, 2011, Art. no. 11.
- [42] C.-C. Chang and C.-J. Lin, "LIBSVM: A library for support vector machines," *ACM Trans. Intell. Syst. Technol.*, vol. 2, pp. 27-1–27-27, 2011, software available at <http://www.csie.ntu.edu.tw/~cjlin/libsvm>
- [43] N. Butt, G. Campbell, Y. Malhi, M. Morecroft, K. Fenn, and M. Thomas, "Initial results from establishment of a long-term broadleaf monitoring plot at Wytham Woods, Oxford, UK," University Oxford, Oxford, U.K., Rep., 2009. [Online]. Available: <http://ctfs.sci.edu/Public/plotdataaccess/TermsConditions.php?plotid=30&typedata=tree>
- [44] J. P. Hoffbeck and D. Landgrebe, "Effect of radiance-to-reflectance transformation and atmosphere removal on maximum likelihood classification accuracy of high-dimensional remote sensing data," in *Proc. Int. Geosci. Remote Sens. Symp. Surf. Atmos. Remote Sens.: Technol., Data Anal. Interpretation*, 1994, vol. 4, pp. 2538–2540.
- [45] H.-R. Y. Sun-Hwa Kim, Jung-Il Shin, and K.-S. Lee, "Effect of atmospheric correction for the land cover classification using hyperspectral data," presented at the Asian Conf. Remote Sensing, Ulaanbaatar, Mongolia, 2006.
- [46] I. Jolliffe, *Principal Component Analysis*. Hoboken, NJ, USA: Wiley, 2002.
- [47] X. Yuan and J. Yang, "Sparse and low-rank matrix decomposition via alternating direction methods," 2009, to be published.
- [48] H. Hu, J. Feng, C. Yu, and J. Zhou, "Multi-class constrained normalized cut with hard, soft, unary and pairwise priors and its applications to object segmentation," *IEEE Trans. Image Process.*, vol. 22, no. 11, pp. 4328–4340, Nov. 2013.
- [49] J.-B. Féret and G. P. Asner, "Semi-supervised methods to identify individual crowns of lowland tropical canopy species using imaging spectroscopy and lidar," *Remote Sens.*, vol. 4, no. 8, pp. 2457–2476, 2012.
- [50] F. E. Fassnacht *et al.*, "Comparison of feature reduction algorithms for classifying tree species with hyperspectral data on three central European test sites," *IEEE J. Sel. Topics Appl. Earth Observ. Remote Sens.*, vol. 7, no. 6, pp. 2547–2561, Jun. 2014.
- [51] R. G. Pontius Jr and M. Millones, "Death to kappa: Birth of quantity disagreement and allocation disagreement for accuracy assessment," *Int. J. Remote Sens.*, vol. 32, no. 15, pp. 4407–4429, 2011.
- [52] NEWFOR, "Alpine space programme, European territorial cooperation 2007–2013-project newfor," 2012. [Online]. Available: <http://www.newfor.net/projet/>
- [53] L. Eysn *et al.*, "A benchmark of LiDAR-based single tree detection methods using heterogeneous forest data from the alpine space," *Forests*, vol. 6, no. 5, pp. 1721–1747, 2015.
- [54] E. Puttonen, P. Litkey, and J. Hyppä, "Individual tree species classification by illuminated–shaded area separation," *Remote Sens.*, vol. 2, no. 1, pp. 19–35, 2009.
- [55] G. Tochon *et al.*, "On the use of binary partition trees for the tree crown segmentation of tropical rainforest hyperspectral images," *Remote Sens. Environ.*, vol. 159, pp. 318–331, 2015.
- [56] C. A. Baldeck and G. P. Asner, "Improving remote species identification through efficient training data collection," *Remote Sens.*, vol. 6, no. 4, pp. 2682–2698, 2014.



Juheon Lee received the B.A. degree from Seoul National University, Seoul, South Korea, and the M.Phil. in atmospheric science, University of Cambridge, Cambridge, U.K., in 2010 and 2012, respectively. He is currently working toward the Ph.D. degree at the Department of Plant Sciences, University of Cambridge.

Since 2012, he has been with the Department of Applied Mathematics and Theoretical Physics, and Plant Sciences, University of Cambridge. His research interests include image processing and its application to geophysics, remote sensing and biomedical imaging.



Xiaohao Cai received the M.S. degree in mathematics from Zhejiang University, Hangzhou, China, in 2008, and the Ph.D. degree in mathematics from The Chinese University of Hong Kong, Hong Kong, in 2012.

He is currently a Postdoctoral Researcher at the Mullard Space Science Laboratory, University College London, London, U.K. He was a Postdoctoral Researcher with the Department of Plant Sciences, and the Department of Applied Mathematics and Theoretical Physics, University of Cambridge, Cambridge, U.K., during May 2014–December 2016, and with the University of Kaiserslautern, during September 2012–May 2014. His research interests include image processing, numerical analysis and their applications in medical imaging, remote sensing, and radio interferometry, etc.



Jan Lellmann received the degrees in computer science and mathematics, and the Doctoral degree from Heidelberg University, Heidelberg, Germany, in 2006, 2007, and 2011, respectively.

He is a Professor in applied mathematics at the Institute for Mathematics and Image Computing, University of Lübeck, Lübeck, Germany. After spending four years as a Postdoctoral Researcher and Leverhulme Early Career Fellow with the Cambridge Image Analysis Group, University of Cambridge, he became a Full Professor at the University of Lübeck in 2015. His research interests include modeling application-specific prior knowledge in image processing, in order to develop methods that are more accurate and require less data. He is particularly interested in high-dimensional problems that are nondifferentiable, or where a number of discrete decisions has to be made, such as the image segmentation problem. Application areas include processing and analysis of images, videos, as well as general two- and higher-dimensional data, such as directional, tensor-, or height data in medicine, biology, and earth sciences.



Michele Dalponte received the M.Sc. degree in telecommunications engineering and the Ph.D. degree in information and communication technologies from the University of Trento, Trento, Italy, in 2006 and 2010, respectively.

He was a Postdoctoral Researcher with the Norwegian University of Life Sciences, Norway, and with the University of Cambridge, U.K. He is currently a Researcher at the Forest Ecology and Biogeochemical Cycles Group, Research and Innovation Center, Edmund Mach Foundation, San Michele all'Adige, Italy. His research interests include the field of remote sensing, in particular the analysis of hyperspectral, multispectral and LIDAR data for forest monitoring. His work has been published in international journals and presented at international conferences. He is a Reviewer for many remote sensing journals.



Nathalie Butt is an Australian Research Council Fellow at the Centre of Excellence for Environmental Decisions, the University of Queensland, Qld, Australia. She works at the interface of climate and ecosystem science.

Her research interest include the vulnerability of species and ecosystems to climate change, and forest response and biophysical feedbacks to land cover change.

Mike Morecroft is an Environmental Scientist working for the nature conservation agency for England.



Carola-Bibiane Schönlieb received the degree in mathematics from the University of Salzburg, Salzburg, Austria, in 2004 and the Ph.D. degree in mathematics from the University of Cambridge, Cambridge, U.K., in 2009.

She is a Reader in Applied and Computational Analysis, the Head of the Cambridge Image Analysis Group, the Department of Applied Mathematics and Theoretical Physics (DAMTP), University of Cambridge, Cambridge, U.K. Moreover, she is the Director of the Cantab Capital Institute for the Mathematics of Information, Cambridge, U.K., the Codirector of the EPSRC Centre for Mathematical and Statistical Analysis of Multimodal Clinical Imaging, a Fellow of Jesus College, Cambridge, U.K., and Coleader of the IMAGES network. After one year of Postdoctoral activity at the University of Göttingen, Germany, she became a Lecturer in DAMTP, promoted to the Reader in 2015. She is an internationally acknowledged Researcher in applied and computational mathematics with particular focus on variational methods for image analysis and image reconstruction, including work on biomedical imaging, remote sensing and image inpainting. She has active interdisciplinary collaborations with clinicians, biologists, physicists, art conservators, chemical engineers, and plant scientists.



Yadvinder Malhi is a Professor of Ecosystem Science at Oxford University, Oxford, U.K.

His research interests include the dynamics and physiology of forests and how they respond to change. He maintains the 18-ha-plot at Wytham Woods that is the focus of this study.



David A. Coomes has been with the staff of the Department of Plant Sciences, Cambridge University, Cambridge, U.K., since 2000. He is the Head of the Forest Ecology and Conservation Group.

His current interests research include modeling the impacts of anthropogenic global change using large-scale forest inventories, and developing approaches for mapping forest change using airborne remote sensing technologies.